Taylor & Francis
Taylor & Francis Group

Science and Technology for the Built Environment

ISSN: 2374-4731 (Print) 2374-474X (Online) Journal homepage: https://www.tandfonline.com/loi/uhvc21

Are aircraft acceleration-induced body forces effective on contaminant dispersion in passenger aircraft cabins?

Hossam A. Elmaghraby, Yi Wai Chiang & Amir A. Aliabadi

To cite this article: Hossam A. Elmaghraby, Yi Wai Chiang & Amir A. Aliabadi (2019) Are aircraft acceleration-induced body forces effective on contaminant dispersion in passenger aircraft cabins?, Science and Technology for the Built Environment, 25:7, 858-872, DOI: 10.1080/23744731.2019.1576457

To link to this article: https://doi.org/10.1080/23744731.2019.1576457

Accepted author version posted online: 31 Jan 2019.
Published online: 06 May 2019.

Science and Technology for the Built Environment, (2019) **25**, 858–872

ISSN: 2374-4731 print / 2374-474X online
DOI: 10.1080/23744731.2019.1576457

Taylor & Francis
Taylor & Francis Group

Are aircraft acceleration-induced body forces effective on contaminant dispersion in passenger aircraft cabins?

HOSSAM A. ELMAGHRABY, YI WAI CHIANG, and AMIR A. ALIABADI*

School of Engineering, University of Guelph, RICH 2515, Guelph, ON N1G 2W1, Canada

Numerical simulations for the effect of body forces due to aircraft acceleration on the airflow and contaminant dispersion in a model for a passenger aircraft cabin are performed in this study. Sulfur hexafluoride (SF_6) was used as the in-cabin contaminant and served as a surrogate for cough particles in the size from 1.6 to 3.0 μm. It was found that those body forces have a significant impact on the contaminant dispersion phenomena and concentrations, especially during the climb leg, where the time-integrated concentration was 2.4 to 2.8 times its counterpart during the steady level (cruise) flight case at the two monitoring locations for most of the simulation time. However, the exposure to the contaminant did not change appreciably during the descent leg. Air velocities, on the other hand, increased noticeably during the climb and descent legs, leading to evident changes in the airflow patterns, airflow circulation magnitude, and, at some locations, airflow circulation directions. The current study has limitations, requiring detailed calculations while considering parametric variations. The findings warrant a closer investigation into the effects of body forces due to aircraft acceleration on the airflow and contaminant dispersion in various passenger aircraft cabins.

Introduction

Billions of people every year prefer to use air travel than other means of transport (Air Transport Action Group 2018). This is because of the fast and reliable service the airliners provide. However, the environment inside a commercial aircraft cabin provides a fertile ground for deterioration of air quality and disease transmission among passengers if proper measures are not taken (Elmaghraby et al. 2018).

In the past two decades, numerous studies with different research approaches have investigated air quality in aircraft cabin environments using air distribution systems as a control measure. These approaches range from purely experimental (Waters et al. 2002; Strøm-Tejsen et al. 2007; Sze To et al. 2009; Li et al. 2014; Fang et al. 2015) to entirely computational (numerical simulations) (Lin et al. 2005; Wan et al. 2009; Hassan 2016) or combinations of both (Zhang et al. 2009; Poussou et al. 2010; Zhang et al. 2012; Isukapalli et al. 2013; Li et al. 2016).

Aircraft are moving with high speeds and accelerations, accomplishing distinct flight mission legs (or intervals) with different dynamic conditions, such as takeoff, climb, cruise, descent, and landing (Hull 2007). Nevertheless, no study in the literature has considered the effect of the resulting body forces from those accelerations on the flow of ventilation air and contaminant dispersion inside aircraft cabins.

The main objective of this work is to fill the gap in the literature that has always considered that passenger aircraft are at rest or under cruise conditions and that the ventilation airflow, buoyancy effects due to occupant-generated thermal plumes, and contaminant dispersion within their cabins are only influenced by gravitational acceleration. The effect of the accelerations induced by the body forces acting on a typical passenger aircraft (Boeing 767-300), such as lift and drag, in addition to the thrust of the jet engines and the weight of the aircraft itself, on the air distribution and gaseous contaminant dispersion inside an economy cabin section is investigated through computational fluid dynamics (CFD) simulations using ANSYS FLUENT software. This is inspired by the existence of the body force term in the Navier-Stokes conservation equations, which in turn can affect the airflow and contaminant dispersion in the aircraft cabin. The mission legs during which the simulations are performed are climb, steady level (cruise), and descent.

Methods

Simulated cabin geometry

The aircraft cabin model used for the current study is adopted from the literature, more specifically, an

Received May 23, 2018; accepted January 16, 2019
Hossam A. Elmaghraby, is a PhD Student. **Yi Wai Chiang, PhD, PEng**, is an Assistant Professor. **Amir A. Aliabadi, PhD, PEng**, is an Assistant Professor.
*Corresponding author email: aliabadi@uoguelph.ca
Color versions of one or more of the figures in the article can be found online at www.tandfonline.com/icnv.

experimental study (Sze To et al. 2009) and the numerical simulation follow-up work (Wan et al. 2009).

The cabin mock-up resembles an actual size sectional economy-class cabin of a Boeing 767 passenger aircraft with 21 seats arranged in three rows (the seven abreast or 2–3–2 seat arrangement). The external dimensions of the cabin mock-up are 4.9 m × 3.2 m × 2.1 m (*W*, *L*, *H*). The cabin mock-up is located at the International Centre for Indoor Environment and Energy, Technical University of Denmark, Lyngby, Denmark. The cabin mock-up appeared for the first time in Strøm-Tejsen et al. (2007), where more details about its configuration and control systems can be found.

The experiments conducted by Sze To et al. (2009) were concerned with the dispersion and deposition of expiratory particles in the aircraft cabin mock-up after being released under different cabin airflow rates. They positioned 15 heated cylinders on the seats to mimic passengers, and they developed an in-house droplet generator to simulate a coughing person (droplet release point). The size distribution of released cough droplets was measured using the interferometric Mie imaging technique combined with an aerosol spectrometer (GRIMM, model 1.108). Additionally, deposition of expiratory droplets in the cabin was measured by the fluorescence dye technique employing several bright dyes depositing on sheets of aluminum foil and polyethylene film. On the other hand, airflow patterns were characterized using the particle image velocimetry technique with a double-pulsed Nd:YAG illumination laser source of 532 nm wavelength and a dual-frame CCD camera.

Figure 1 shows a three-dimensional view for the created cabin model in the current study to the exact dimensions using the design software DesignModeler included in the ANSYS 17.0 CFD package and a plan view for the seats.

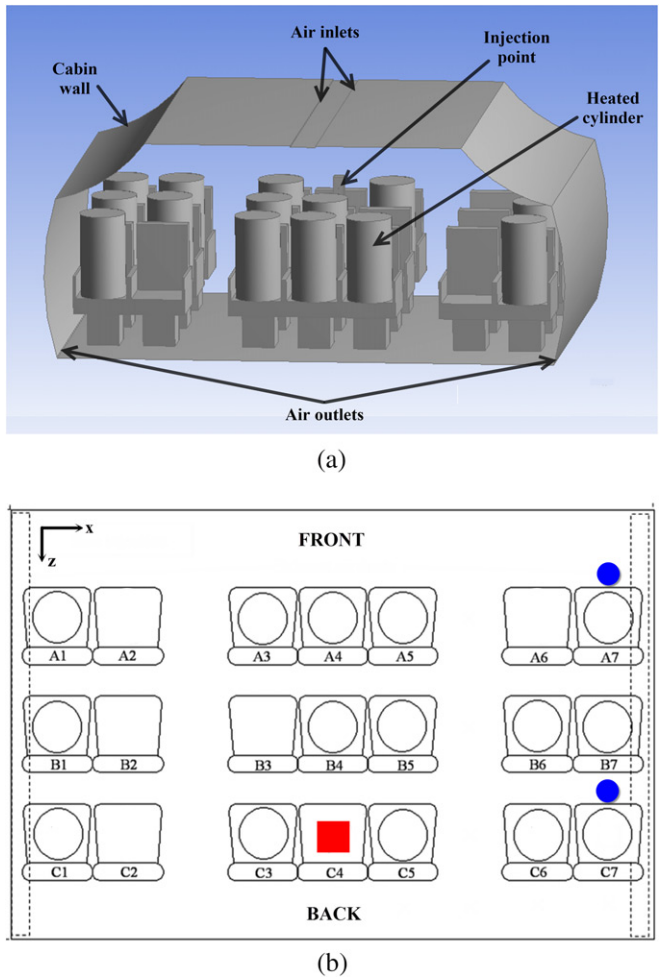

Fig. 1. The computational cabin model used in the current study: a. three-dimensional view of the geometry built in ANSYS and b. plan view for the cabin with the cougher/injector position (red square) and the SF_6 concentration monitoring points (blue circles).

Governing equations

The equations governing airflow and contaminant dispersion in the current cabin model solved by the ANSYS FLUENT 18.2 software are as follows:

(a) The mass conservation (continuity) equation:

$$\frac{\partial \rho}{\partial t} + \nabla.(\rho \vec{V}) = 0, \tag{1}$$

where ρ is the in-cabin air density, t is the time, and $\vec{V}$ is the flow velocity vector. Because the density ρ in the model is constant (independent of space and time), except where buoyancy effects are accounted for, the continuity equation simplifies to the kinematic condition that the velocity field should be *solenoidal* or *divergence-free* (Aliabadi 2018):

$$\nabla.(\vec{V}) = 0. \tag{2}$$

This is because the airflow in the cabin can be safely considered incompressible as verified by considering the dimensionless Mach number. Even with the highest velocity in the domain equal to the cough velocity of 10.6 m s^{-1}, the highest Mach number in the cabin is 10.6/343 = 0.03, which is much less than the incompressibility assumption limit (Ma = 0.3).

(b) The momentum conservation equation:

$$\frac{\partial}{\partial t}(\rho \vec{V}) + \nabla.(\rho \vec{V}\vec{V}) = -\nabla p + \nabla.(\bar{\bar{\tau}}) + \rho \vec{g} + \rho \vec{a}, \tag{3}$$

where p is static pressure, $\bar{\bar{\tau}}$ is the stress tensor, and $\vec{g}$ and $\vec{a}$ are the gravitational and external body accelerations, respectively (ANSYS Inc. 2015).

(c) The energy equation:

$$\frac{\partial}{\partial t}(\rho E) + \nabla.\left(\vec{V}(\rho E + p)\right) = \nabla.\left(k_{eff}\nabla T - \sum_j h_j \vec{J}_j + \left(\bar{\bar{\tau}}_{eff}.\vec{V}\right)\right) + S_h, \tag{4}$$

where k_{eff} is the effective conductivity = $k + k_t$ (k_t is the turbulent thermal conductivity), T is the temperature, $\vec{J}_j$ is the diffusion flux of species j, and S_h is and additional volumetric heat source (e.g., passenger bodies). E is defined as,

$$E = h - \frac{p}{\rho} + \frac{V^2}{2}, \tag{5}$$

where h is the sensible enthalpy of the fluid flow, which is defined for ideal gases (i.e., air) as,

$$h = \sum_j Y_j h_j,$$

where Y_j is the mass fraction of species j and,

$$h_j = \int_{T_{ref}}^{T} C_{p,j} dT.$$

For the pressure solver used, T_{ref} is taken as 298.15 K (ANSYS Inc. 2015).

(d) Species transport equation:

$$\frac{\partial}{\partial t}(\rho Y_i) + \nabla.\left(\rho \vec{V} Y_i\right) = -\nabla.\vec{J}_i + S_i, \tag{6}$$

where Y_i is the local mass fraction of each species i in the domain, and S_i is the rate of creation (or consumption) of species by addition (or removal) from the dispersed phase plus any user-defined sources. $\vec{J}_i$ is the diffusion flux of species i, which for mass diffusion in turbulent flows is defined as,

$$\vec{J}_i = -\left(\rho D_{i,m} + \frac{\mu_t}{Sc_t}\right)\nabla Y_i - D_{T,i}\frac{\nabla T}{T}, \tag{7}$$

where $D_{i,m}$ is the mass diffusion coefficient for species i in the mixture, $D_{T,i}$ is the thermal (Soret) diffusion coefficient, μ_t is the turbulent viscosity, and Sc_t is the turbulent Schmidt number.

(e) Turbulence kinetic energy (k) and turbulence kinetic energy dissipation rate (ε) equations (renormalization group [RNG] k-ε model):

$$\frac{\partial}{\partial t}(\rho k) + \frac{\partial}{\partial x_i}(\rho k u_i) = \frac{\partial}{\partial x_j}\left(\alpha_k \mu_{eff}\frac{\partial k}{\partial x_j}\right) + G_k + G_b - \rho\varepsilon + S_k, \tag{8}$$

and

$$\frac{\partial}{\partial t}(\rho \varepsilon) + \frac{\partial}{\partial x_i}(\rho \varepsilon u_i) = \frac{\partial}{\partial x_j}\left(\alpha_\varepsilon \mu_{eff}\frac{\partial \varepsilon}{\partial x_j}\right) + C_{1\varepsilon}\frac{\varepsilon}{k}(G_k + C_{3\varepsilon}G_b) - C_{2\varepsilon}\rho\frac{\varepsilon^2}{k} - R_\varepsilon + S_\varepsilon, \tag{9}$$

where α_k and α_ε are the inverse effective Prandtl numbers for k and ε, respectively; S_k and S_ε are user-defined source (or sink) terms; and $C_{1\varepsilon}$, $C_{2\varepsilon}$, and $C_{3\varepsilon}$ are constants defined by the RNG k-ε model theory. In addition, G_k represents the generation (or consumption) of turbulence kinetic energy due to the mean velocity gradients, and G_b is the generation (or consumption) of turbulence kinetic energy due to buoyancy, which is formulated using the standard gradient diffusion hypothesis as,

$$G_b = -\,g_i\frac{\mu_t}{\rho Pr_t}\frac{\partial \rho}{\partial x_i},$$

where g_i is the component of the gravitational vector in the ith direction, μ_t is the turbulent viscosity, and Pr_t is the turbulent Prandtl number.

Model boundary and initial conditions

The model's boundary and initial conditions found in the reference studies (Sze To et al. 2009; Wan et al. 2009) were closely followed and implemented in the numerical solver FLUENT 18.2 for the case of 200 L s^{-1} supply airflow rate. This was the only supply airflow rate considered through the conventional mixing ventilation system used. For more information on the conventional mixing ventilation system strategy in commercial aircraft cabins, the reader is referred to more detailed studies (Mangili and Gendreau 2005; Elmaghraby et al. 2018).

For simulation, sulfur hexafluoride (SF_6) gas was released in the cabin to mimic the injection and transport of the cough's smallest size droplets (typically 1.6–3.0 µm) and that formed the largest number concentration of the injected droplet ensemble in the experiments. This was performed for the sake of model validation and considering that the current study is a preliminary concept study and not an exact one. This is to avoid the high computational burden that comes with simulating particle motion. Table 1 shows the boundary and initial conditions for the current model.

The simulation time for the transient airflow part is 350 s at the start of which the cough (SF_6 release) was introduced for 1 s with a released air volume of 0.4 L. Before this transient run, the airflow domain was completely solved in the steady mode.

Additionally, the standard wall functions were used for near-wall flow treatment with all of the turbulence models employed, and the SIMPLE solution algorithm was used for the pressure–velocity coupling.

For the spatial discretization scheme, the least squares cell-based method was used for the gradient, the second-order method was employed to solve the pressure, and the second-order upwind method was used to solve all other equations (momentum, species, turbulence, energy, etc.). On the other hand, for the temporal discretization, the first-order implicit method (implicit backward Euler method) was employed for the transient part of the simulation following a fixed time stepping procedure with a timestep size of 0.1 s while allowing 10 solution iterations per time step.

To accurately simulate cough particle deposition on walls and surfaces, the SF_6 gas was not allowed to bounce off the walls and surfaces in the cabin model. This was accomplished by setting a surface reaction boundary condition at every wall and surface to dissociate SF_6 upon contact with sulfide (S_2) and fluorine (F_2) gases according to the following reaction:

$$2SF_6 \overset{at\ wall}{\longrightarrow} S_2 + 6F_2. \tag{10}$$

Because the released SF_6 in the cabin is already at very low concentrations, the concentrations of the sulfide and fluorine gases produced from its dissociation are extremely

Table 1. Boundary and initial conditions for the model.

Boundary and initial conditions	Value
Supply air temperature	24 °C
Supply airflow rate	200 L s^{-1} (corresponds to a supply velocity of 2.61 m s^{-1})
Supply air absolute humidity	0.92 g kg^{-1} (corresponds to 5% relative humidity at supply air temperature)
Cabin wall temperature	18 °C
Heating cylinder heat release	60 W per cylinder (person)
SF_6 (cough) injection location	Seat C4
Air velocity at injection location	10.6 m s^{-1}

low and do not affect the air composition, fluid properties, or monitored SF_6 concentration in the cabin.

This method allows economic computation of surrogate simulation of small particles that behave like gases. Assessment of this method is carried out in the subsection on model validation and error estimation.

Grid independence test

To define the degree of independence of the obtained solution (airflow velocity and time-averaged SF_6 concentration) from the grid size changes, a grid independence test was conducted. In the present work, four levels of grid fineness (sizes) were created—coarse grid (4,704,751 elements), medium grid (5,522,517 elements), fine grid (7,375,800 elements), and very fine grid (9,761,227 elements)—in the order of grid element size decrease or fineness increase. The grid refinement ratio (r) between each two consecutive grid levels was kept constant at 1.1. The unstructured grid consists mainly of tetrahedron, wedge, and hexahedron elements. The tetrahedron elements were used to fill the majority of the cabin interior volume, and wedge and hexahedron-shaped elements were mainly used to create seven layers of inflation mesh adjacent to the cabin walls and around the seats and cylinders to capture the flow boundary layer more efficiently at these positions. The y^+ value was kept between 300 and 400 at the walls by forcing an average thickness for the first inflation mesh layer of 0.1 m. This is backed by several studies in the literature (Blocken et al. 2007; Aliabadi et al. 2018).

Transient simulation runs were performed for airflow and SF_6 dispersion in the cabin on each grid level with the identical boundary conditions mentioned previously. Figure 2 presents the normalized SF_6 concentration time series (real-time concentration divided by time-averaged concentration) as they change with the simulation time for the four grid levels with respect to the experimental data (see next subsection). The real-time SF_6 concentration was monitored at the breathing level of the occupants (1.17 m) at seats A7 and C7 (blue circles in Figure 1).

In addition to the graphical comparison of solution on the four grid levels, the grid convergence index (GCI) was calculated to indicate the amount of asymptotic convergence that the solution achieved by determining the uncertainty in

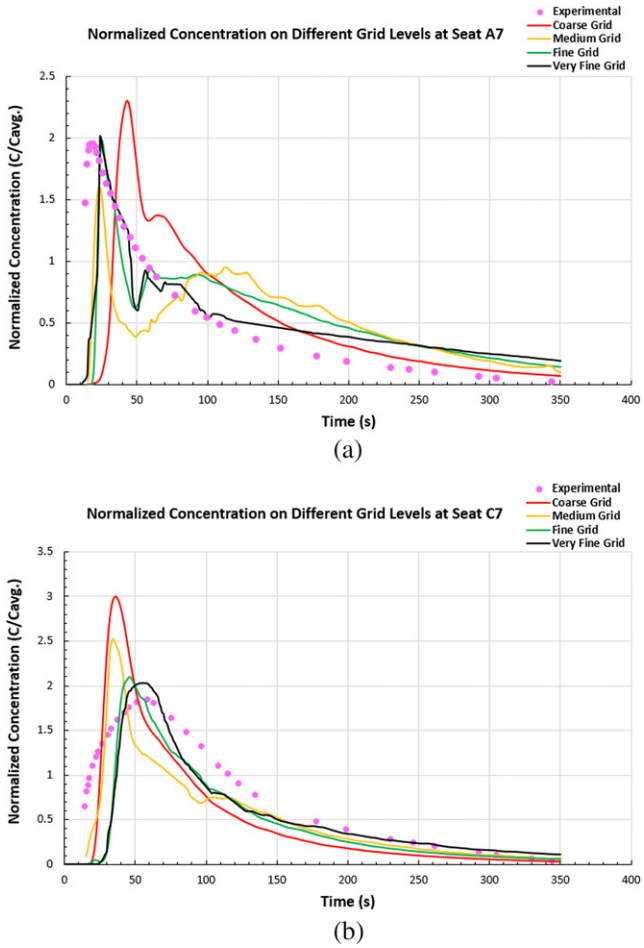

Fig. 2. Normalized SF_6 concentration change with simulation time on the four grid levels used: a. at seat A7 and b. at seat C7.

solution between two consecutive grid levels (Roache 1994; Aliabadi 2018).

In the current study, the GCI is calculated between two consecutive grid levels m and n using the following formula:

$$GCI_{mn} = \frac{F_s|\epsilon_{mn}|}{r^p - 1}, \tag{11}$$

where F_s is a factor of safety recommended to be 3.0 for

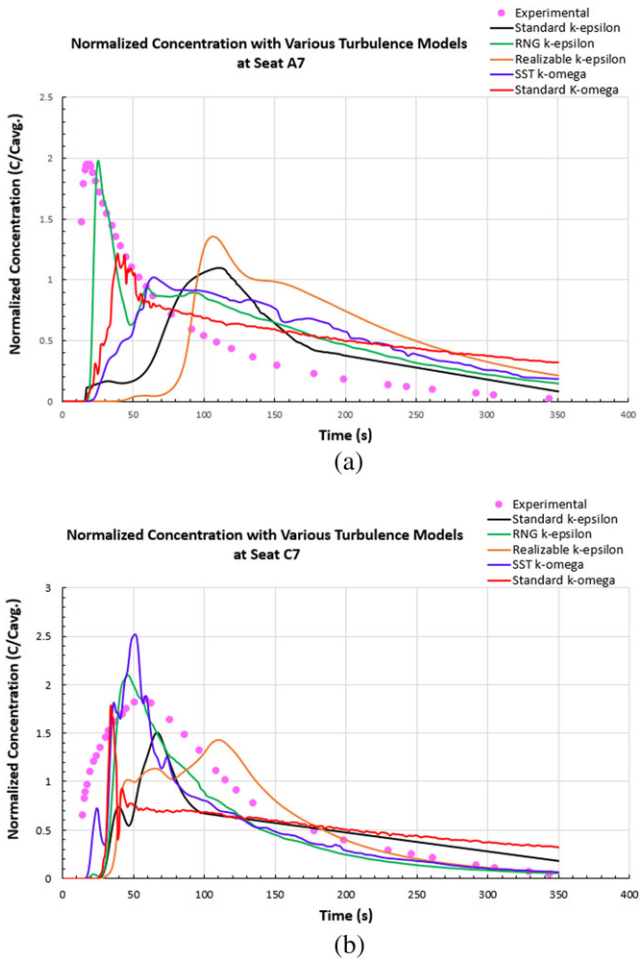

Fig. 3. Comparison of the normalized SF_6 concentration time series between the experiment and numerical simulations on the fine grid level using different turbulence models: a. at seat A7 and b. at seat C7.

comparisons of two meshes and 1.25 for comparison of three meshes (such as in the current model), ϵ_{mn} is relative error between the two solutions obtained on the two consecutive grid levels, and p is the order of convergence. For more information on the calculation procedure followed, refer to more detailed references (Aliabadi 2013, 2018).

The GCI for SF_6 concentration calculations from coarse to medium grids was 3.13%, from medium to fine grids was 1.26%, and from fine to very fine grids was 0.34% at seat A7. On the other hand, at seat C7, the GCI was 3.55% from coarse to medium grids, 1.41% between medium and fine grids, and 0.29% between fine and very fine grids. Based on these results, and because the change in the solution between the fine and very fine grid levels is minimal, the fine grid level was found to exhibit enough grid independency of the solution while preserving computational economy. Therefore, the fine grid level was used.

Model validation and error estimation

The experimental data used for the aircraft cabin model validation were mainly extracted from the original study (Sze To et al. 2009) considering the smallest particle size range

Table 2. FB and NMSE values for the numerical predictions of the turbulence models used.

	Seat A7		Seat C7	
Turbulence model	FB	NMSE	FB	NMSE
Standard k-ε	0.67455	1.25019	0.55768	0.58504
RNG k-ε	0.31867	0.71138	0.39909	0.37711
Realizable k-ε	0.69038	1.53628	0.50152	0.58732
SST k-ω	0.60606	1.19904	0.31138	0.25556
Standard k-ω	0.49237	0.97809	0.51303	0.55494

Note: SST - Shear Stress Transport; RNG - Re-Normalization Group.

(1.6–3.0 μm) to be compared with the SF_6 gas (passive tracer) concentration time series monitored at the two seats A7 and C7 over the simulation time. The SF_6 gas was chosen as a surrogate to the smallest size cough particles because of its high density and molecular weight (about 6.14 kg m^{-3} and 146.06 g mol^{-1}, respectively), which make it capable of mimicking the movements of those particles in the cabin. Additionally, this choice is based on the findings of multiple studies in the literature that indicate that the smallest size droplets (3 μm in diameter and less) behave like heavy gaseous substances (especially SF_6) when dispersing in the cabin space (Zhang et al. 2009; Li et al. 2014). To mimic particle deposition at the walls, it was necessary to have an SF_6 sink at the walls by implementing a dissociation mechanism at the wall boundary. Such a need was confirmed by comparing the results without a dissociation mechanism, in which case the SF_6 concentrations in the domain were too high.

Figure 3 depicts the compared normalized SF_6 concentration time series at seats A7 and C7 using the numerical solution obtained on the fine grid only and employing different turbulence models from the Reynolds-averaged Navier-Stokes group that can simulate buoyancy effects on the production and dissipation of turbulence kinetic energy (k).

The error estimation in the current CFD model predictions for concentration time series are calculated using a procedure first proposed by Steven Hanna (1989) and used by him and others later in multiple studies to express the error between the observed and predicted concentrations in atmospheric air quality models (Chang and Hanna 2004; Hanna and Chang 2012; Aliabadi et al. 2017). This procedure uses two performance measures to express the error, the fractional mean bias (FB) and the normalized mean square error (NMSE), defined as follows,

$$FB = \frac{2\left(\overline{C_o C_p}\right)}{\left(\overline{C_o} + \overline{C_p}\right)} \tag{12}$$

$$NMSE = \frac{\left(\overline{(C_o C_p)^2}\right)}{\left(\overline{C_o} * \overline{C_p}\right)}, \tag{13}$$

where C_o and C_p are the observed and predicted concentrations, respectively. Whereas FB is a measure of the shift between the observed and predicted quantities, NMSE is a

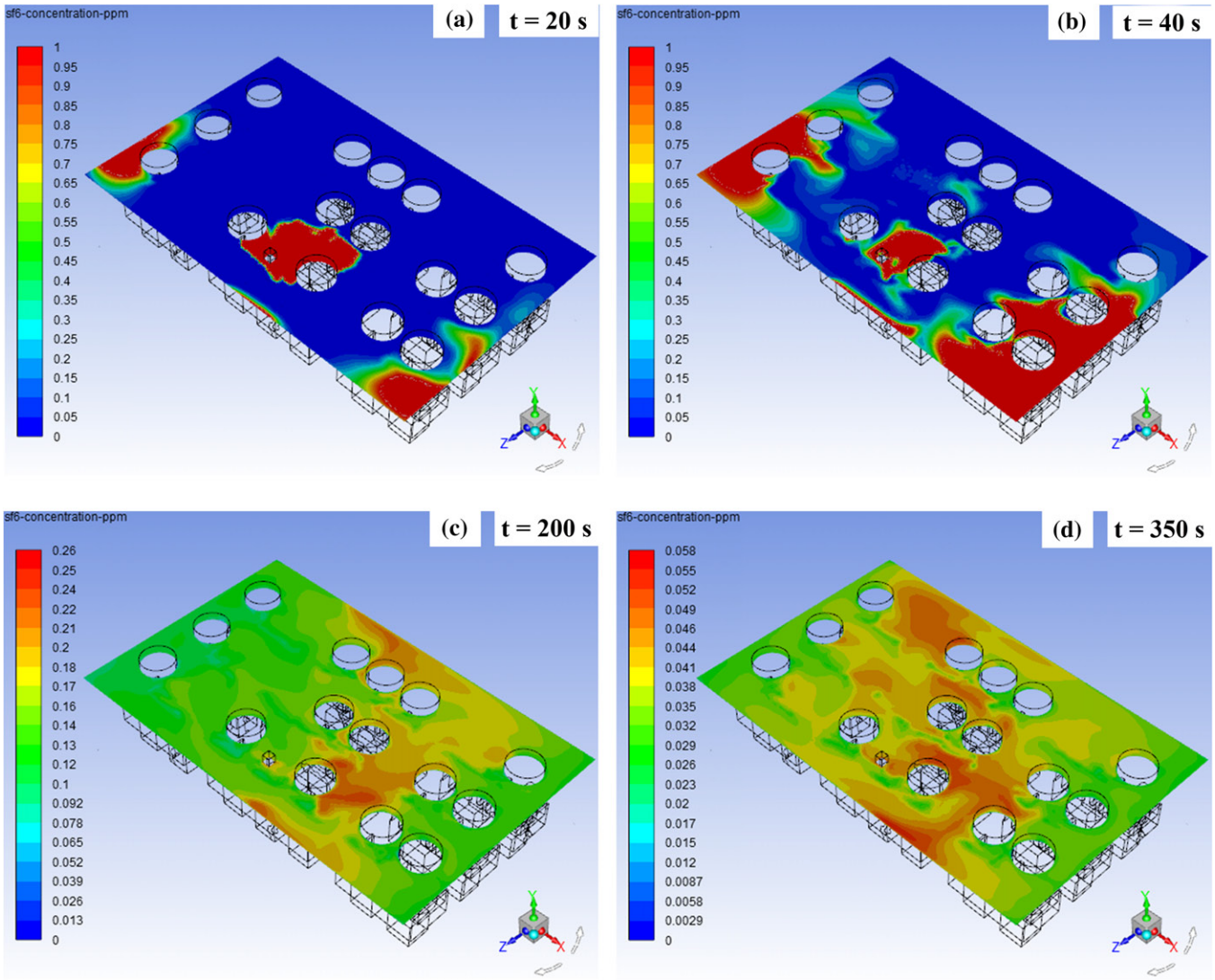

Fig. 4. SF_6 concentration contour plots at breathing level during steady level flight: a. at t = 20 s, b. at t = 40 s, c. at t = 200 s, and d. at t = 350 s after cough release.

measure of the spread between observed and predicted quantities. For a perfect model, FB and NMSE are both equal to zero (Chang and Hanna 2004).

Table 2 gives the FB and NMSE values calculated for the normalized SF_6 concentration time series between the experimental measurements and the numerical predictions of the same turbulence models as in Figure 3.

From Table 2, it can be concluded that the RNG *k*-ε turbulence model exhibits the overall lowest values for FB and NMSE at both seats among all other models. Consequently, the RNG *k*-ε model provides the most accurate SF_6 concentration predictions at both seats A7 and C7 and was therefore used. This result also agrees with the recommendations for similar airflow simulation cases in closed spaces found in the literature (Chen 1995; Zhai et al. 2007; Zhang et al. 2007; Wang and Chen 2009; Liu et al. 2013). On the other hand, the NMSE values for normalized concentration at seat C7 are about 50% less than those at seat A7, whereas FB values are almost the same at both seats. This shows that the shift between the observed and predicted concentration values is similar, but the spread of the predicted data with respect to the observed ones is two times higher at seat A7, which indicates less accurate predictions.

For all turbulence models used, the decrease in prediction accuracy from seat C7 to seat A7 can very well be attributed to the condition of airflow, and therefore that of the surrogate SF_6 gas, from the emission source (at seat C4) to each seat. From C4 to C7 the flow is mainly lateral and is less susceptible to the bulk flow turbulence than the primarily longitudinal flow experienced from C4 to A7 (see Figure 1).

Generally, the calculated FB and NMSE figures agree well with the graphical presentation for the measured and calculated concentration time series (see Figure 3).

The experimental measurements of droplet concentration and the resulting passenger exposure (see the subsection on effect of aircraft body forces on contaminant dispersion)

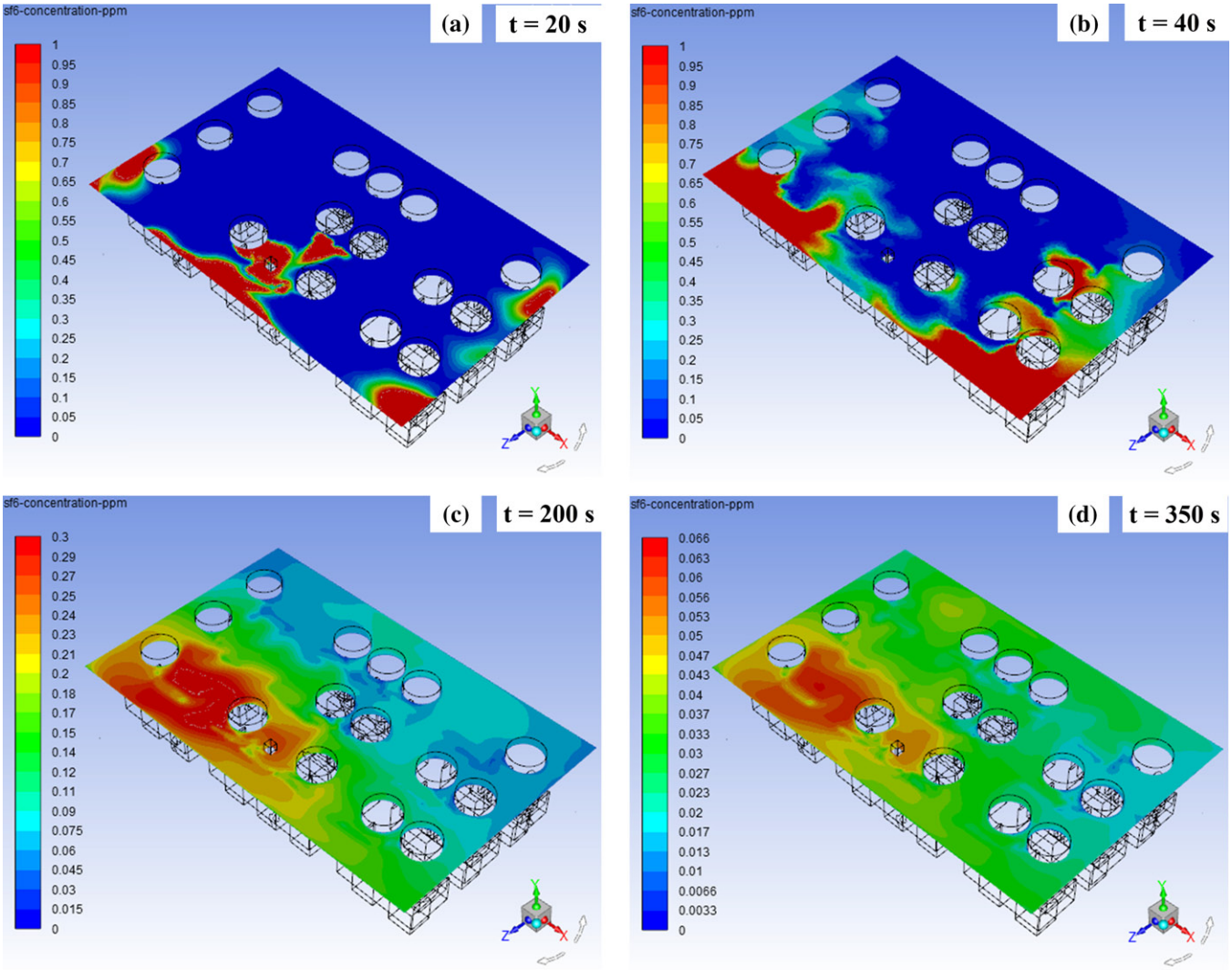

Fig. 5. SF_6 concentration contour plots at breathing level during climb: a. at t = 20 s, b. at t = 40 s, c. at t = 200 s, and d. at t = 350 s after cough release.

were not free from error and uncertainty. This uncertainty was mainly caused by the limited resolution of the aerosol spectrometer used and that of the liquid flow meter in the droplet generator. The uncertainty in exposure was estimated to be $\pm 9.63 \times 10^{-6}$ mL for droplets $\leq$15 μm in diameter, which formed the majority of droplets captured in the experiments (Sze To et al. 2009). Despite those estimations, no error bars were provided for the experimental droplet concentration time series (shown as pink dots in Figures 2 and 3) by the authors of the original study.

Calculation of aircraft body acceleration components

The aircraft vertical acceleration (a_v) and horizontal acceleration (a_h) components were calculated during climb and descent legs using a basic approach adapted from different sources in aircraft dynamics literature (University of Southampton 2005; Gudmundsson 2013; National Aeronautics and Space Adminstration 2015).

The calculation procedure relies on applying Newton's second law ($\sum \vec{F} = m\vec{a}$) on two axes passing through the center of gravity of the aircraft; one is vertical and the other is horizontal. The forces in action are the lift (L), drag (D), aircraft weight (W), and thrust of the jet engines (T).

For example, the relative vertical acceleration on the aircraft cabin during a climb is found to be equal to 2.4 g, which is composed of two parts; 1.4 g due to aircraft acceleration and 1 g representing the gravitational component. More information on the calculation procedure followed can be found in the Appendix at the end of this paper.

Results and discussion

Effect of aircraft body forces on contaminant dispersion

The climb and descent simulations were run for the same time span of the steady level flight simulations (350 s) but with the new acceleration components resulting from the

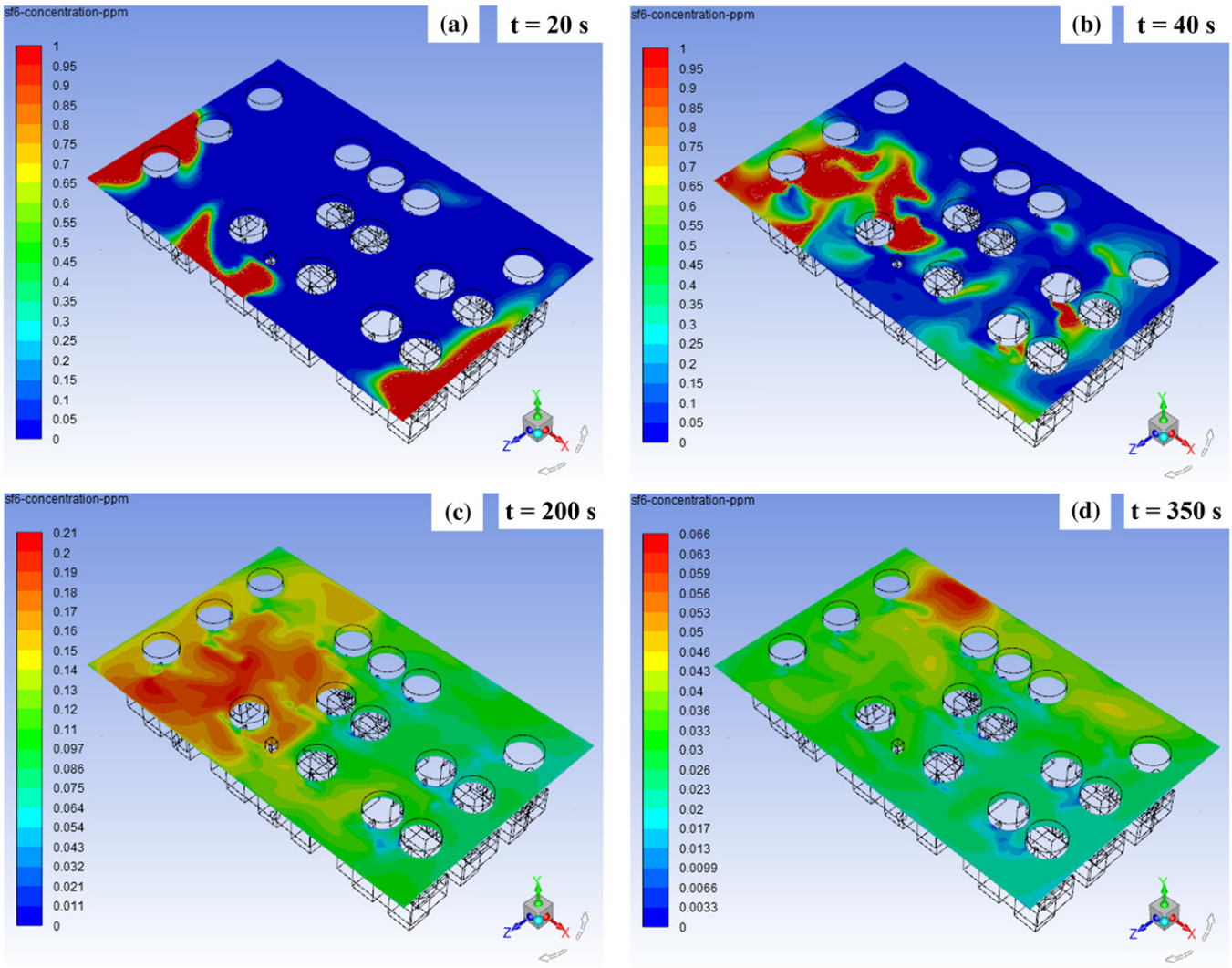

Fig. 6. SF_6 concentration contour plots at breathing level during descent: a. at t = 20 s, b. at t = 40 s, c. at t = 200 s, and d. at t = 350 s after cough release.

climb and descent calculations implemented in the numerical solver. Figures 4, 5, and 6 depict the SF_6 concentration contours in the cabin at different simulation times during the steady level flight, climb, and descent legs, respectively.

Looking at Figure 4, one can notice that the SF_6 dispersion starts from the central rear area, where the cougher is located, and then the contaminant tends to disperse laterally to the two sides with a high concentration region preserved at the center. Next, and specifically after around 200 s has passed since the cough was released, the dispersion pattern changes from lateral to longitudinal where the SF_6 spreads to the front rows. This steady level flight dispersion pattern is clearly motivated only by the airflow in the cabin with no existent body forces (other than gravity) on the aircraft that can manipulate the contaminant dispersion, which kept it at the center of the cabin for most of the simulation time.

On the other hand, the body forces during the climb leg force the SF_6 to mainly disperse to the rear of the cabin as seen in Figure 5. SF_6 moves to the back in a longitudinal pattern just after being released and then disperses laterally to the sides while being restricted to the back rows. Later, a minor longitudinal dispersion pattern drives some of the released contaminant to the front rows starting from left to right while keeping the majority of the contaminant at the back left corner where the highest risk of exposure exists (to be assessed later in this section).

The body forces during the descent leg were also effective on the SF_6 dispersion pattern in the cabin as seen in Figure 6. The contaminant is pushed to the rear of the cabin for a short time due to its own inertia before the descent body forces make it disperse to the front rows while restricting its lateral movement to the left side of the cabin. Later, SF_6 disperses slightly to the right side of the cabin while concentrating mainly at the left side of the front row (note that the cabin occupancy is not symmetric from left to right).

Generally, the body forces due to aircraft acceleration during the climb and descent legs seem to influence the

dispersion pattern of the SF_6 contaminant surrogate in the cabin. The contaminant is forced to disperse in directions of the body force vector and to settle at either the rear (climb) or front (descent). This behavior is mainly influenced by the airflow patterns in the cabin throughout the different flight legs (investigated later in the following subsection).

For the two set monitoring locations at seats A7 and C7, Figure 7 shows a comparison of the calculated concentration time series of SF_6 during steady level flight, climb, and descent.

It can be clearly noticed from Figure 7 that the tracer gas concentration is significantly higher (up to 150%–300% more) during the climb leg than the steady level flight case for most of the simulation time, especially at seat A7. Consequently, the level of exposure (which can be interpreted from the area under the curves) of passengers sitting at both seats significantly increases throughout the aircraft climb time. This poses greater risks to the health and well-being of most passengers in the cabin upon exposure to hazardous gaseous substances, in-cabin contaminants, or some infectious particulates during the aircraft climb leg that can take up some considerable time for some flights and aircraft models.

On the other hand, the SF_6 concentration time series during the descent leg does not noticeably differ from that for the steady level flight time, possibly due to lower accelerations induced by body forces. This indicates that the level of passenger exposure to contaminants is almost identical between the descent and the steady level flight scenarios at breathing height.

To put the comparisons between climb, descent, and steady level flight in more quantitative form, the exposure of passengers to the simulated contaminant concentration over time is assessed by calculating the area under the curve corresponding to each case of the three scenarios at seats A7 and C7 using the following integral:

$$Exposure = \int_0^{350\ s} C_{SF_6}(t)\ dt, \tag{14}$$

where $C_{SF_6}(t)$ is the time-dependent SF_6 concentration for each case in parts per million, and the unit for the calculated exposure is Parts per million second.

Both the composite trapezoidal rule and composite Simpson's rule were employed to obtain approximate solutions for the exposure integral being applied to the irregular concentration time series in Figure 7. Table 3 shows the ratio of passenger exposure during each of the climb and the descent legs to that during the steady level flight and the ratio of exposure during the climb leg to the descent leg at seats A7 and C7.

Looking at Table 3, it can be noted that passenger exposure is always highest during the climb leg when compared to the steady level flight and descent legs. The most elevated exposure ratio was 3.0 to 1, calculated between climb and descent at seat C7. At the same seat, passenger exposure during the descent leg was slightly less than the steady level flight with a ratio of 0.9 to 1.

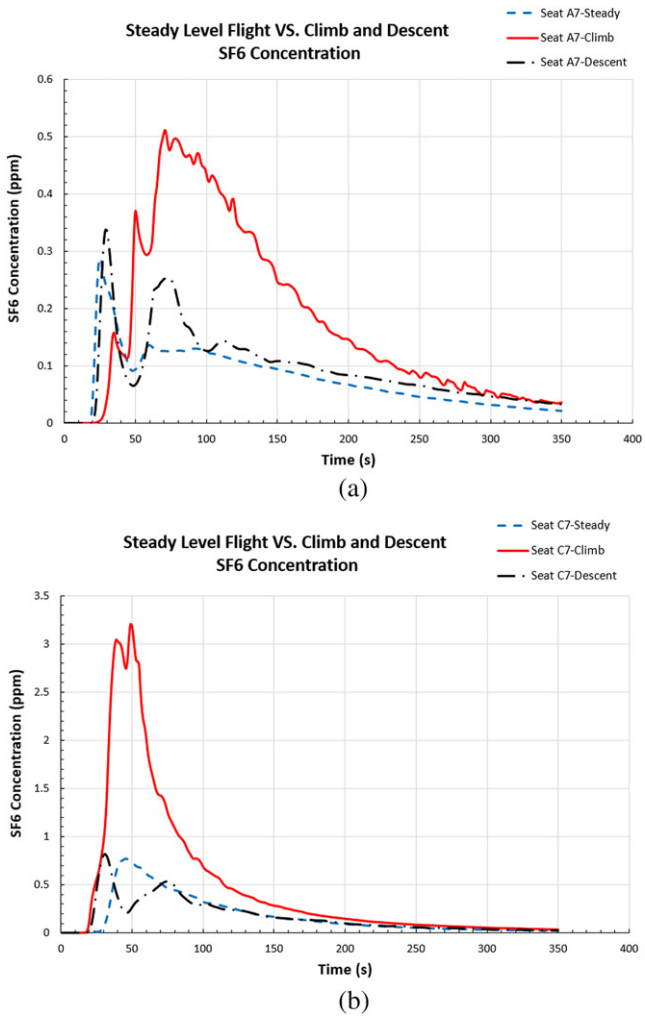

Fig. 7. Comparison of the predicted SF_6 concentration time series among steady level flight, climb, and descent scenarios: a. at seat A7 and b. at seat C7.

Table 3. Ratio of passenger exposure between different flight legs at the two monitoring locations.

Seat	Flight leg	Passenger exposure ratio
A7	Climb : Steady level flight	2.4:1
	Descent : Steady level flight	1.3:1
	Climb : Descent	1.9:1
C7	Climb : Steady level flight	2.8:1
	Descent : Steady level flight	0.9:1
	Climb : Descent	3.0:1

At seat A7, however, the climb to steady flight exposure ratio was higher than the ratio between the climb and descent legs, whereas the exposure during the descent was almost identical to that during steady flight with a ratio of 1.3 to 1.

One factor that may have contributed to the considerable difference in the SF_6 concentration time series (or exposure) between the climb and descent legs is the difference between climb and descent rate of velocity change and the

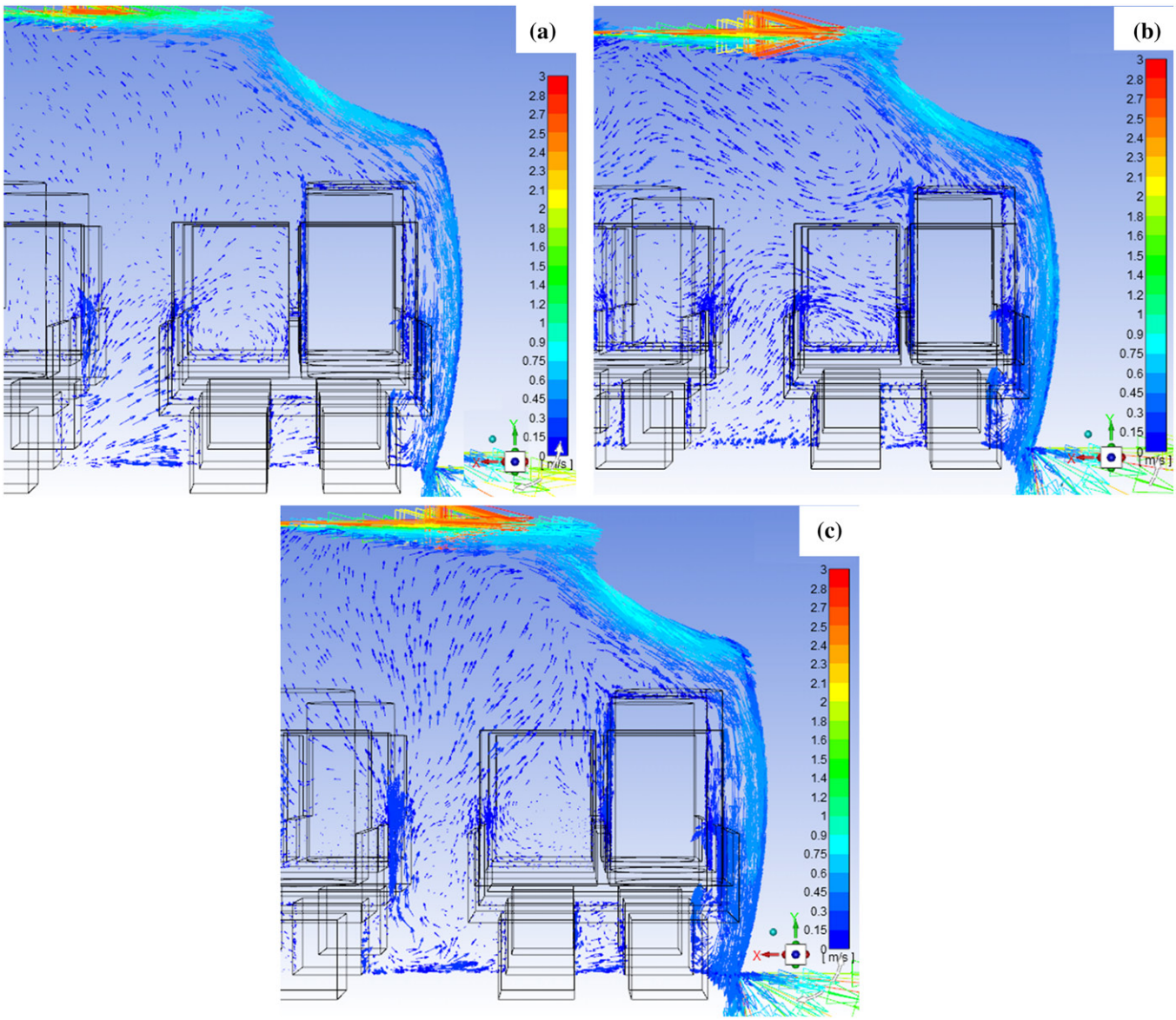

Fig. 8. Airflow velocity vectors near the wall: a. during steady level flight, b. during climb, and c. during descent.

corresponding accelerations. The climb speed for most modern jet-powered passenger aircraft can reach up to 600 km h^{-1} (324 knots) or more, whereas the full-powered descent rate is limited to around 250 km h^{-1} (135 knots) to ensure passenger comfort. This large difference in aircraft speed between the two mission legs yields dissimilar aircraft accelerations and therefore distinct effects of the generated body forces on the contaminants dispersion rates and flow patterns inside the cabin.

Another factor in play is the difference between the climb and descent (inclination) angles. During the take-off and climb legs, most jet-powered passenger aircraft adopt an inclination angle from 15° to 20°; such an angle is much steeper than the small descent angle restricted mostly to 3° to perform comfortable descents. In addition to the rise in aircraft speed, the increase in climb angle over the descent angle can also contribute to enhancing the dispersion rate of contaminants and changing their distribution contours within the cabin. This is because changing the flight path angles significantly alters the values of body force components acting on the aircraft in motion and the contained air on the vertical and horizontal directions and therefore the aircraft acceleration components in each of those two directions. Such effects were fully considered in the present model.

Effect of aircraft body forces on airflow patterns and circulation

In addition to the effects that body forces have on contaminant dispersion inside the cabin, they affect the airflow patterns, and such patterns can be quantified using both airflow velocity fields and circulation in the cabin. Figure 8 shows the airflow velocity vector field near the wall on a lateral

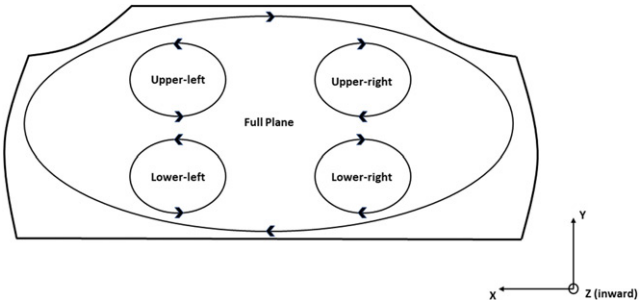

Fig. 9. Example of the followed notation for estimating the airflow circulation on the full $x-y$ plane (Γ_z) and its four quadrant corners.

plane at the middle of the cabin during the steady level flight, climb, and descent legs.

Mean airflow velocity magnitudes in all directions inside the cabin were in general greater during climb and descent than that throughout steady level flight. The monitored airflow velocity magnitudes for the simulated flight times increased anywhere between 1% and 45% during climb and between 6% and 42% during descent with respect to the steady level flight air velocity magnitudes. On the other hand, the air velocity components (V_x, V_y, and V_z) exhibited different values of increase and decrease between climb and steady flight and between descent and steady flight, with no fixed trend.

The increase in airflow velocity magnitudes throughout the climb and descent legs changed the airflow patterns in the cabin to some degree. One form of this change is the increased air boundary layer thickness adjacent to the cabin walls due to the tendency of the air to separate from the walls as it moves downward during climb and descent. In other words, the increased downward airflow velocities (0.9 m s^{-1} for climb and 0.8 m s^{-1} for descent compared to 0.65 m s^{-1} during steady level flight) led to reduced airflow attachment to the walls. Consequently, the strongest downward flow separation (thickest airflow boundary layer) was noticed during climb.

Another effect that the airflow velocity changes have on airflow patterns is the alteration of the airflow circulation in the cabin. For circulating flows, such as the highly turbulent airflow in the cabin space, circulation (Γ) is defined as the line integral around a closed curve of the velocity field

$$\Gamma = \oint_{\partial s} \vec{U}.d\vec{l}. \tag{15}$$

Figure 9 shows examples of arbitrary airflow circulation paths on the $x-y$ plane set at the middle of the cabin.

Due to cabin symmetry along the longitudinal aircraft axis, these circulation paths are considered to represent the tendency of airflow to circulate throughout the cabin. From the figure, it can be clearly seen that the airflow circulation can be considered on the full planes, such as $x-y$, $x-z$, and $z-y$ planes ($x-z$ and $z-y$ planes are not shown in the figure but correspond to circulations Γ_y and Γ_x, respectively), and also at the four quadrant corners of each plane, namely, the upper left, upper right, lower left, and lower right corners. This was made possible by calculating the average airflow velocities on separate line segments located at the top, bottom, right, left, and center (horizontally and vertically) of each of the mentioned planes. Afterwards, the difference in magnitude between each pair of those velocities, the distances between each two parallel lines on which they were calculated, and the surface area of the plane on which the circulation is quantified were used to yield an approximate circulation on each plane as follows,

$$\Gamma_x = \left(\frac{\Delta v_z}{\Delta y} - \frac{\Delta v_y}{\Delta z}\right)\Delta y \Delta z, \tag{16a}$$

$$\Gamma_y = \left(\frac{\Delta v_x}{\Delta z} - \frac{\Delta v_z}{\Delta x}\right)\Delta x \Delta z, \tag{16b}$$

$$\Gamma_z = \left(\frac{\Delta v_y}{\Delta x} - \frac{\Delta v_x}{\Delta y}\right)\Delta x \Delta y. \tag{16c}$$

Table 4 presents the calculated circulation on the full planes and the four quadrant corners of each plane during the steady level flight, climb, and descent legs and the percentage change in those values when each of the climb and descent legs is compared to the steady level flight case.

Studying Table 4, it can be noted that the circulation on the full planes, in the three directions, and their four quadrant corners exhibits both increases and decreases during climb and descent, with respect to the steady level flight case, with increases occurring more frequently. However, those increases are not exclusive to one flight leg and occur almost equally between climb and descent.

One unique characteristic of circulation is that the change in the direction of rotation can be shown between steady level flight and climb and between steady level flight and descent, in addition to the increase or decrease in the circulation strength (magnitude). This is exhibited by a change in the sign of the circulation from positive (clockwise direction) to negative (counterclockwise direction) and vice versa, following the right-hand rule. These cases are also clearly demonstrated in Table 4 (footnote d) to show that a change in the direction of airflow rotation occurs whether the circulation magnitude increases or decreases.

The greatest increase in circulation, taking the steady level flight case as a reference, is seen on the upper right corner during descent on the $x-z$ plane (Γ_y) with around a 498% increase. This is followed by the climb on the lower left corner of both the $y-z$ and $x-z$ planes with 249.2% and 243.9% increases, respectively.

One may also notice that on the full plane, and in every direction, the circulation strength during the climb and descent legs similarly increases or decreases from the steady flight case, even with different percentages, but this is not a common trend on the four quadrant corners.

Another interesting observation is that the circulation on the $x-y$ plane (Γ_z) only exhibits a decrease during both the climb and descent legs on the full plane, whereas on the four quadrant corners it always shows an increase during those two legs.

Table 4. Airflow circulation values and changes between steady level flight, climb, and descent legs.[a]

Plane/side corner	Flight leg	Circulation (m^2 s^{-1})[b]			Change in circulation during climb or descent[c] (%)		
		Γ_x	Γ_y	Γ_z	Γ_x	Γ_y	Γ_z
Full plane	Steady flight	−0.0215	−0.0959	0.0419	–	–	–
	Climb	−0.0555	−0.1554	0.0148	**158.1**	62.05	−64.64
	Descent	0.0690	−0.2854	0.0392	**221.1**[d]	**197.7**	−6.45
Lower right corner	Steady flight	0.0392	−0.0869	0.3846	–	–	–
	Climb	−0.0469	−0.0572	0.4522	19.64[d]	−34.13	17.59
	Descent	0.1024	−0.1022	0.4174	**161.3**	17.71	8.53
Lower left corner	Steady flight	0.0326	−0.0254	−0.3260	–	–	–
	Climb	0.1137	−0.0872	−0.4275	**249.2**	**243.9**	31.12
	Descent	−0.0294	−0.0076	−0.3575	−9.83[d]	−70.06	9.64
Upper right corner	Steady flight	−0.0433	−0.0226	0.3283	–	–	–
	Climb	−0.1414	0.0095	0.4118	**226.6**	−57.81[d]	25.42
	Descent	0.0639	−0.1351	0.3567	47.49[d]	**498.3**	8.64
Upper left corner	Steady flight	−0.0499	0.0389	−0.3449	–	–	–
	Climb	0.0192	−0.0205	−0.4216	−61.66[d]	−47.39[d]	22.25
	Descent	−0.0679	−0.0405	−0.3774	35.94	3.99[d]	9.41

Note: [a]Values in boldface represent significant percentage changes (greater than 100%).
[b]Positive values indicate a clockwise direction and negative values indicate a counterclockwise direction following the right-hand rule.
[c]Positive values indicate an increase from steady flight and negative values indicates a decrease from steady flight.
[d]Accompanied by a change in the direction of rotation.

Conclusion and future work

In this study, numerical simulations for the effect of body forces due to aircraft acceleration on the airflow and contaminant dispersion (from human cough) in a model for a passenger aircraft cabin are performed. The steady level (cruise) flight leg, which takes most of the flight time, is taken as the reference case to which the contaminant concentration and airflow changes during the climb and descent flight legs are compared.

From the concentration contour plots for the contaminant surrogate (SF_6) it was noticed that the body forces due to aircraft acceleration during the climb and descent legs influence the dispersion patterns of the contaminant surrogate in the cabin. The contaminant was made to disperse in directions of the body force vector and to eventually settle either at the rear of the cabin during climb or at the front during descent until this contaminant is cleared out of the cabin by the ventilation system. This behavior is mainly influenced by the airflow patterns in the cabin throughout the different flight legs. It was also noted that the concentration of the contaminant at the two set monitoring locations, and therefore the passenger exposure, increased substantially during the climb leg from the steady level flight with ratios of 2.4 to 1 and 2.8 to 1 at seats A7 and C7, respectively. However, this was not the case during the descent leg, throughout which the SF_6 concentration did not considerably differ from that during the steady level flight time with exposure ratios limited to 1.3 to 1 at seat A7 and 0.9 to 1 at seat C7.

Airflow velocity magnitudes, on the other hand, increased everywhere in the simulated cabin during climb (between 1% and 45% increase) and descent (between 6% and 42% increase) compared to the steady level flight case. However, this was not the case for the airflow velocity components (V_x, V_y, and V_z), which showed different levels of increase and decrease with no fixed trend.

The change in airflow velocities had a significant effect on the airflow patterns and circulation in the cabin. Downward airflow coming from supply slots was less attached to the cabin walls during climb and descent than through the steady flight time. Additionally, airflow circulation strength in every direction inside the cabin, either on the full plane or its four quadrant corners, exhibits both increases and decreases during climb and descent, with respect to the steady level flight case, with increases occurring more frequently.

The findings indicate the potent effect that acceleration-induced body forces have on the airflow behavior and contaminant dispersion inside the cabins of passenger aircraft and call for more research attention to this topic to unveil some ventilation and/or ergonomic design remedies to the negative effects this may have on the health of occupants of aircraft, trains, and other moving vehicles.

The current study provides a straightforward approach to studying contaminant dispersion under the influence of passenger aircraft acceleration-induced body forces using numerical means and by avoiding complicated and expensive experimental investigations. However, there are some implications for the study that the reader must be aware of. The current investigation is generally a preliminary concept work and not an exact one. SF_6 was used to mimic cough particles of the smallest size range, which results in some inaccuracy. In addition, the results of the study cannot be generalized on all passenger aircraft because a specific aircraft model and

design (Boeing 767-300) was used. Moreover, only a section of the economy cabin was considered for investigation and not the full aircraft fuselage. Lastly, further parametric variations of the variables included in the study, such as contaminant injection point location and/or direction, increasing the frequency of injections, and/or varying the number of concentration monitoring sites and their locations, were beyond the scope of the current study. Such factors may have some impact on the difference in passenger exposure to contaminants between the steady level flight, climb, and descent cases and necessitate further investigations.

The effect of the acceleration-induced body forces on particle dispersion will be investigated in follow-up studies. In addition, larger and more modern cabin models with different configurations will be utilized to generalize the findings of the current study. In addition, both airflow/ventilation design and source control strategies can be employed to reduce the negative effects of contaminant dispersion experienced during the climb leg. Such strategies can include, but are not limited to, changing airflow direction, altering airflow rate, using different ventilation schemes, relocating and/or isolating contamination sources (e.g., coughing persons), changing cough volume/intensity (e.g., by using napkins), and altering cough orientation or direction. For the descent leg, however, the impact of practical future plans such as the one proposed by the European Organisation for the Safety of Air Navigation (EUROCONTROL) in 2011 to implement a continuous descent approach (CDA) instead of the conventional staged descent approach can be studied. The CDA is sought to eliminate the extended low-level thrust segments currently performed in the middle of the descent stages. In addition to controlling contaminant dispersion inside the cabin, CDA may help to offset the harmful effects of passenger aircraft noise and atmospheric emissions (EUROCONTROL 2011).

ORCID

Hossam A. Elmaghraby http://orcid.org/0000-0002-8613-6958
Yi Wai Chiang http://orcid.org/0000-0002-7798-9166
Amir A. Aliabadi http://orcid.org/0000-0002-1002-7536

References

Air Transport Action Group. 2018. *Facts & Figures*. Geneva, Switzerland: Air Transport Action Group.

Airliners. 2017. *Aircraft Technical Data & Specifications/Boeing 767-300*. https://www.airliners.net/aircraft-data/boeing-767-300/104. Accessed May 9, 2017.

Aliabadi, A.A. 2013. *Dispersion of Expiratory Airborne Droplets in a Model Single Patient Hospital Recovery Room with Stratified Ventilation*. Vancouver: The University of British Columbia.

Aliabadi, A.A. 2018. *Theory and Applications of Turbulence: A Fundamental Approach for Scientists and Engineers*. Guelph, ON, Canada: Amir Abbas Aliabadi Publications.

Aliabadi, A.A., E.S. Krayenhoff, N. Nazarian, L.W. Chew, P.R. Armstrong, A. Afshari, and L.K. Norford. 2017. Effects of roof-edge roughness on air temperature and pollutant concentration in urban canyons. *Boundary-Layer Meteorology* 164(2):249–79.

Aliabadi, A.A., N. Veriotes, and G. Pedro. 2018. A very large-eddy simulation (VLES) model for the investigation of the neutral atmospheric boundary layer. *Journal of Wind Engineering and Industrial Aerodynamics* 183:152–71.

ANSYS Inc. 2015. *ANSYS Fluent Theory Guide: Release 16.2*. Canonsburg, PA: SAS IP.

Blocken, B., T. Stathopoulos, and J. Carmeliet. 2007. CFD simulation of the atmospheric boundary layer: Wall function problems. *Atmospheric Environment* 41(2):238–52.

Chang, J.C., and S.R. Hanna. 2004. Air quality model performance evaluation. *Meteorology and Atmospheric Physics* 87(1–3):167–96.

Chen, Q. 1995. Comparison of different *k*-ε models for indoor air flow computations. *Numerical Heat Transfer, Part B: Fundamentals* 28(3):353–69.

Elmaghraby, H.A., Y.W. Chiang, and A.A. Aliabadi. 2018. Ventilation strategies and air quality management in passenger aircraft cabins: A review of experimental approaches and numerical simulations. *Science and Technology for the Built Environment* 24(2):160–75.

EUROCONTROL. 2011. *Continuous Descent: A Guide to Implementing Continuous Descent*. Brussels Belgium: EUROCONTROL.

Fang, Z., H. Liu, B. Li, A. Baldwin, J. Wang, and K. Xia. 2015. Experimental investigation of personal air supply nozzle use in aircraft cabins. *Applied Ergonomics* 47:193–202.

Gudmundsson, S. 2013. *General Aviation Aircraft Design: Applied Methods and Procedures*. Oxford: Butterworth-Heinemann.

Hanna, S.R. 1989. Confidence limits for air quality model evaluations, as estimated by bootstrap and jackknife resampling methods. *Atmospheric Environment* 23(6):1385–98.

Hanna, S.R., and J. Chang. 2012. Acceptance criteria for urban dispersion model evaluation. *Meteorology and Atmospheric Physics* 116(3–4):133–46.

Hassan, M. 2016. *Numerical Investigation of Improving Distribution Systems in Aircraft Passengers Cabins*. Giza, Egypt: Cairo University.

Hull, D.G. 2007. *Fundamentals of Airplane Flight Mechanics*. *Fundamentals of Airplane Flight Mechanics*. New York: Springer.

Isukapalli, S.S., S. Mazumdar, P. George, B. Wei, B. Jones, and C.P. Weisel. 2013. Computational fluid dynamics modeling of transport and deposition of pesticides in an aircraft cabin. *Atmospheric Environment* 68:198–207.

Li, F., J. Liu, J. Pei, C.H. Lin, and Q. Chen. 2014. Experimental study of gaseous and particulate contaminants distribution in an aircraft cabin. *Atmospheric Environment* 85:223–33.

Li, F., J. Liu, J. Ren, X. Cao, and Y. Zhu. 2016. Numerical investigation of airborne contaminant transport under different vortex structures in the aircraft cabin. *International Journal of Heat and Mass Transfer* 96:287–95.

Lin, C.-H., K.H. Dunn, R.H. Horstman, J.L. Topmiller, M.F. Ahlers, J.S. Bennett, L.M. Sedgwick, and S. Wirogo. 2005. Numerical simulation of airflow and airborne pathogen transport in aircraft cabins—Part I: Numerical simulation of the flow field. *ASHRAE Transactions* 111(1):755–64.

Liu, W., J. Wen, C.H. Lin, J. Liu, Z. Long, and Q. Chen. 2013. Evaluation of various categories of turbulence models for predicting air distribution in an airliner cabin. *Building and Environment* 65:118–31.

Mangili, A., and M.A. Gendreau. 2005. Transmission of infections during commercial air travel. *Lancet* 365(9478):2176–7.

National Aeronautics and Space Adminstration. 2015. *Forces in a Climb*. https://www.grc.nasa.gov/www/k-12/airplane/climb.html. Accessed October 10, 2017.

Poussou, S.B., S. Mazumdar, M.W. Plesniak, P.E. Sojka, and Q. Chen. 2010. Flow and contaminant transport in an airliner cabin induced

by a moving body: Model experiments and CFD predictions. *Atmospheric Environment* 44(24):2830–39.
Roache, P.J. 1994. Perspective: A method for uniform reporting of grid refinement studies. *Journal of Fluids Engineering* 116(3):405–13.
Strøm-Tejsen, P., D.P. Wyon, L. Lagercrantz, and L. Fang. 2007. Passenger evaluation of the optimum balance between fresh air supply and humidity from 7-h exposures in a simulated aircraft cabin. *Indoor Air* 17(2):92–108.
Sze To, G.N., M.P. Wan, C.Y.H. Chao, L. Fang, and A. Melikov. 2009. Experimental study of dispersion and deposition of expiratory aerosols in aircraft cabins and impact on infectious disease transmission. *Aerosol Science and Technology* 43(5):466–85.
University of Southampton. 2005. *Weight, Geometry, Lift, Drag and Thrust Properties*. http://www.southampton.ac.uk/~jps7/Aircraft Design Resources/Sydney aerodynamics for students/perf/perf_ac.html. Accessed May 10, 2017.
Wan, M.P., G.N. Sze To, C.Y.H. Chao, L. Fang, and A. Melikov. 2009. Modeling the fate of expiratory aerosols and the associated infection risk in an aircraft cabin environment. *Aerosol Science and Technology* 43(4):322–43.
Wang, M., and Q. Chen. 2009. Assessment of various turbulence models for transitional flows in enclosed environment (RP-1271). *HVAC&R Research* 15(6):1099–1119.
Waters, M.A., T.F. Bloom, B. Grajewski, and J. Deddens. 2002. Measurements of indoor air quality on commercial transport aircraft. *Proceedings of the 9th International Conference on Indoor Air Quality and Climate*, Monterey, CA, June 30–July 5, 2002, pp. 782–87.
Zhai, Z.J., Z. Zhang, W. Zhang, and Q. (Yan) Chen. 2007. Evaluation of various turbulence models in predicting airflow and turbulence in enclosed environments by CFD: Part 1—Summary of prevalent turbulence models. *HVAC&R Research* 13(6):853–70.
Zhang, T.T., P. Li, and S. Wang. 2012. A personal air distribution system with air terminals embedded in chair armrests on commercial airplanes. *Building and Environment* 47(1):89–99.
Zhang, Z., X. Chen, S. Mazumdar, T. Zhang, and Q. Chen. 2009. Experimental and numerical investigation of airflow and contaminant transport in an airliner cabin mockup. *Building and Environment* 44(1):85–94.
Zhang, Z., W. Zhang, Z.J. Zhai, and Q.Y. Chen. 2007. Evaluation of various turbulence models in predicting airflow and turbulence in enclosed environments by CFD: Part 2—Comparison with experimental data from literature. *HVAC&R Research* 13(6):871–86.

Appendix: Procedure for determining the aircraft acceleration components during climb and descent

Climb

Newton's second law is applied on the vertical and horizontal axes shown in the Figure A1.

$$\sum \vec{F} = m\vec{a} \tag{A1}$$

On the vertical axis:

$$T\sin\theta - D\sin\theta + L\cos\theta - W = m\vec{a_v}, \tag{A2}$$

and on the horizontal axis:

$$T\cos\theta - D\cos\theta - L\sin\theta = m\vec{a_h}, \tag{A3}$$

where $\vec{a_v}$ and $\vec{a_h}$ are the vertical and horizontal acceleration components, respectively (Gudmundsson 2013).

The unknowns (T, θ, D, L, m) are estimated based on industrial specifications and dimensions for the Boeing 767-300 aircraft (Airliners 2017): $T = 462.6$ KN (for a twin-jet engine), $\theta = 20°$, $m = 159{,}210$ kg (max. takeoff weight), and $W = mg$.

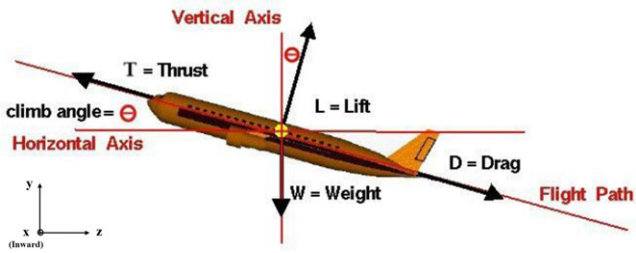

Fig. A1. Forces on a passenger aircraft during climb with the two axes (horizontal and vertical) set for the calculation of acceleration components.

$$D = C_D * 0.5\rho V^2 A, \tag{A4}$$

$$L = C_L * 0.5\rho V^2 A, \tag{A5}$$

where C_D and C_L are the drag and lift coefficients, respectively; ρ is the air density; V is the aircraft velocity (taken as 155 m s^{-1}); and A is the reference (wing) area. The drag coefficient is given as

$$C_D = C_{D_0} + kC_L^2, \tag{A6}$$

where C_{D_0} is the part of drag coefficient due to friction and pressure on the aircraft body, and k is a constant that incorporates the other part of the drag coefficient due to lift (lift induced drag) (University of Southampton 2005). $C_D = 0.06$ (approximation for many aircraft aerofoils). The constant is

$$k = \frac{1}{\pi\ AR\ e}, \tag{A7}$$

where e is equal to 0.85 for twin-engine wide-body aircraft, and AR is the wing aspect ratio which is determined from

$$AR = \frac{(\text{wing span})^2}{\text{wing area}} = \frac{(47.57)^2}{283.3} = 7.987. \tag{A8}$$

These yield $k = 0.04688$. Taking $C_{D_0} = 0.017$ for a twin-engine wide-body aircraft and substituting in Equation A6 yields $C_L = 0.96$. Substituting in Equations A4 and A5 and assuming the density of atmospheric air to be 1.2 kg m^{-3},

$$D = 229.473\ \text{KN},$$

and

$$L = 3671.568\ \text{KN}.$$

Substituting in Equations A2 and A3, the vertical and horizontal components of the aircraft acceleration are, respectively,

$$\vec{a_v} = 13.79\ \text{ms}^{-2} = -1.4\ \vec{g},$$

and

$$\vec{a_h} = -7.14\ \text{ms}^{-2} = 0.73\ \vec{g}.$$

Lastly, the absolute acceleration components calculated are expressed in the form of relative acceleration components on

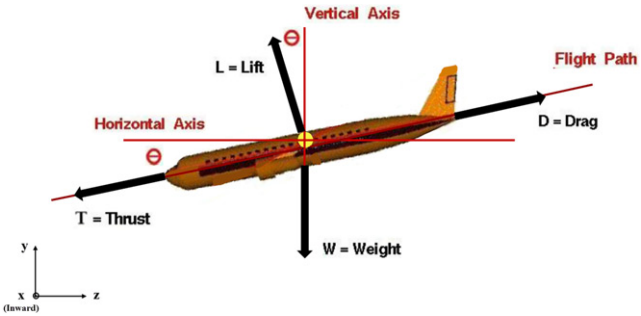

Fig. A2. Forces on a passenger aircraft during descent with the two axes (horizontal and vertical) set for the calculation of acceleration components.

the air inside the aircraft cabin before being implemented in FLUENT. This is attained by reversing the sign of each acceleration component and superimposing it on any acceleration(s) that may exist in the same direction (e.g., gravity). This is justified by Newton's third law and yields the relative acceleration components as follows,

$$\vec{a_y} = (-13.79-9.81) = -23.6\ \text{ms}^{-2} = 2.4\ \vec{g},$$
$$(\text{or } 23.6\ \text{ms}^{-2} \text{ acting downwards})$$

and

$$\vec{a_z} = 7.14\ \text{ms}^{-2} = -0.73\ \vec{g}.$$
$$(\text{or } 7.14\ \text{ms}^{-2} \text{ acting toward the tail of the aircraft}).$$

Descent

For descent, the same procedure and parameters for climb apply, but the aircraft velocity (V) and the descent angle (θ) are adjusted to the new case. $V = 70\ \text{m s}^{-1}$ (full-powered descent), and $\theta = 3°$. With the aircraft tilted downward as in Figure A2, Equations A2 and A3 are changed.

On the vertical axis:

$$L\cos\theta + D\sin\theta - T\sin\theta - W = m\vec{a_v}, \quad \text{(A9)}$$

and on the horizontal axis:

$$L\sin\theta + T\cos\theta - D\cos\theta = m\vec{a_h}. \quad \text{(A10)}$$

Substituting in Equations A4 and A5 with the new velocity and using the same values for C_D and C_L, ρ, and A,

$$D = 49.974\ \text{KN},$$

and

$$L = 799.586\ \text{KN}.$$

Substituting the D and L values (keeping T and m the same) in Equations A9 and A10 yields the vertical and horizontal components of aircraft acceleration during descent.

$$\vec{a_v} = -4.9303\ \text{ms}^{-2} = 0.50\ \vec{g},$$

and

$$\vec{a_h} = 2.85\ \text{ms}^{-2} = -0.29\vec{g}.$$

Finally, the relative acceleration components are calculated for the descent leg using the same approach previously followed for the climb leg.

$$\vec{a_y} = (4.9303-9.81) = -4.88\ \text{ms}^{-2} = 0.49\ \vec{g}$$
$$(\text{or } 4.88\ \text{ms}^{-2} \text{ acting downwards})$$

and

$$\vec{a_z} = -2.85\ \text{ms}^{-2} = 0.29\ \vec{g}$$
$$(\text{or } 2.85\ \text{ms}^{-2} \text{ acting toward the head of the aircraft}).$$